Visualization of travelling waves propagating in a plate equipped with 2D ABH using wide-field holographic vibrometry

Laure Lagny, Mathieu Secail-Geraud, Julien Le Meur, Silvio Montrésor, Kevin Heggarty, Charles Pezerat, Pascal Picart

Visualization of travelling waves propagating in a plate equipped with 2D ABH using wide-field holographic vibrometry

Laure LAGNY[a,b], Mathieu SECAIL-GERAUD[a,b,c], Julien LE MEUR[d], Silvio MONTRESOR[a,b], Kevin HEGGARTY[d], Charles PEZERAT[a,b,c], Pascal PICART[a,b,c]

[a] Laboratoire d'Acoustique de l'Université du Mans, LAUM - UMR 6613 CNRS, Le Mans Université, Avenue Olivier Messiaen, 72085 LE MANS CEDEX 9, France

[b] Institut d'Acoustique - Graduate School, Le Mans Université, CNRS, Avenue Olivier Messiaen, 72085 LE MANS CEDEX 9, France

[c] ENSIM, Ecole Nationale Supérieure d'Ingénieurs du Mans, rue Aristote, 72085 LE MANS CEDEX 09, France

[d] IMT Atlantique Bretagne – Pays de la Loire, Campus de Brest, Département d'Optique, Technopole Brest-Iroise, CS 83818, 29285 BREST, France

Corresponding author: pascal.picart@univ-lemans.fr

Abstract

This paper presents a method for wide-field vibrometry based on high-speed digital holographic interferometry. We demonstrate the possibility of measuring transient vibrations of structures at 100kHz frame rate when providing 46600 quantitative data on 380cm^2 rectangular spot at the object surface. Investigation of traveling acoustic waves propagating in alloy plate equipped with a two-dimensional acoustic black hole (ABH) is considered. Such a structure leads to localized vibrations of high amplitude and constitutes a good candidate for methodology testing. The wave front is generated by a short shock with duration about 50µs. The time sequence of the vibration field obtained after the shock is depicted and exhibits the propagation of the wave front in the plate and inside the ABH. It follows that the observation of the modification of the wave propagation can be observed at very short time scale. The modification of the wave front due to the gradient in elastic properties related to the ABH area is also highlighted.

1. Introduction

The development of lightweight structures is a field of research with many issues and significant impacts. At present, several main reasons lead manufacturers to move towards a reduction of weight in automobile, aeronautics, railway, etc., in order to reduce their energy consumption. In this context, lightweight structures build with wave traps such as acoustic black holes (ABH) are serious candidates to develop non-resonant structures without adding any mass. The ABH concept was first proposed by Mironov [1] and Krylov [2]. In the past years, several research groups have developed research on the analysis, modelling and the characterization of ABH performance. Experimental evidence of the vibration reduction induced by 1D ABH (beam termination) or 2D ABH (pit of power law profile embedded in a plate) have been shown in [3,4]. The main features of the 1D ABH effect can be investigated from the measurement of the reflection coefficient of a beam termination [5] and from its modelling based on wave expansion [6], or wavelets expansion [7]. Spiral ABH have also

been proposed to reduce the size of the tapered region [8]. The 2D ABH trap effect linked to the capture of the ray trajectories of flexural waves and the focalization effect has been investigated in [9,10] and the scattering of the 2D ABH has been modeled in [11]. The wave propagation in plates with multiple ABH indentations or ABH grids have also been modelled and measured in [12,13]. Taking advantage of the vibration damping induced by ABH without adding mass, first propositions of transfer of the ABH concept towards industrial applications have been made [14,15]. More recently, geometrical [16] and impact [17] non linearity inside the ABH have been exploited to transfer energy from the low frequency range (defined as being below the ABH cut-on frequency, ~500-600Hz) to high frequencies. Such strategy improves the ABH performance in the low frequency domain, in which ABH is not active. Such nonlinear systems require analysis in the time domain, in which the present metrological tool can be useful. Especially, one might be interested by characterizing their global behavior when submitted to transient excitation or to investigate their nonlinear properties. From the point of view of measurement and metrology, the challenge is to get characterization at both the time and space scale of the involved phenomena. Generally, in the domains of acoustics, vibro-acoustics, vibrations of structures or flow-induced vibrations, Laser Doppler Vibrometer (LDV) is the most used tool for dynamic measurements [18-21]. Its main drawback is that the measurement is pointwise and a collection of data points at the surface of the object has to be obtained using scanning. Such scanning may be quite long, typically about 4h to scan a surface with 41×41 points. In order to overcome scanning, multipoint vibrometers were developed to simultaneously yield a collection of data points at the surface of the inspected object [22-26]. Nevertheless, a high density of data points can be obtained by digital holographic techniques. By this way, the required measurement time can be reduced when simultaneously getting high number of data points. In the past, time-averaging in digital holography was discussed as an efficient tool for vibration analysis [27-34]. Full object movement was also demonstrated through stroboscopic recordings [35-44]. However, in most of these studies, the excitation of structures was performed in the stationary regime. As mentioned before, studying complex structures equipped with wave traps requires analysis at both their time and space scales. It follows that providing a real-time follow-up of the vibration amplitude under arbitrary excitation conditions is a challenge for full-field optical metrology.

During the past years, the performances of continuous wave lasers with power larger than 5W, and high-speed imaging sensors (frame rate up to 1MHz) have been significantly improved. Merging these technologies into holographic techniques yields an adapted

approach for real-time and multi-point recording of transient phenomena in complex media. When recording digital holograms with a high-speed sensor, recording transient phenomena at both their time and space scales becomes possible. Recently [45,46], the authors demonstrated the ability of digital holography as an accurate multipoint vibrometer. Identification of the force distribution at the surface of a vibrating object, by solving a regularized inverse problem, was discussed when exciting with monochromatic signals [47]. In this paper, we aim at considering the case of transient excitations of structures and observation over a large field of view, typically larger than 350cm^2. In literature, there does not exist any experimental set-up to provide the wide-field visualization of the interaction between transient waves and 2D ABH. Indeed, the use of a scanning laser Doppler vibrometer is not adapted to this case because it requires spatial scanning and a perfect reproduction of the impact to the structure for each scan. In the case of scanning with 41×41 data points, that would require 1681 impacts. A perfect repeatability for such a number of impacts is really not possible. When recording the wave front propagation at its time and space scale by wide-field and time-resolved digital holography, the problem of the reproducibility of impact is naturally bypassed.

However, the spatial resolution in measurement results is also a key parameter. When increasing the frame rate of any high-speed sensor, the available spatial resolution has to be decreased consequently. In addition, the spatial resolution in the reconstructed images from holograms closely depends on the number of useful pixels at recording and on the sensor-to-scene distance. So, there is contradiction between wide-field (the scene has to be far from sensor) and high spatial resolution (the frame rate has to be decreased). In this paper, on-line configuration for digital holography is optimized so as to make the most of the capabilities of both sensor and digital holography. A negative zoom is designed in order to fulfill the Shannon requirements of holographic recording, and to provide the maximum occupation of the reconstructed image of the scene in the field of view. From the reconstructed images, the Doppler phase can be extracted and yields data related to the transient wave front propagation. Furthermore, the light efficiency is optimized by using a dedicated diffractive optical element for the surface illumination, providing a maximization of photon collection at the sensor plane. Digital holography is an appropriate measurement method for capturing vibrations varying rapidly with space and time. Such configuration is the one of an ABH which justify the application case discussed in this paper. In the case presented in this paper, one aims at visualizing the transient acoustic wave front propagating in a plate equipped with a 2D ABH, and excited by a 50µs short shock from an impact hammer. The interest for the ABH leads in

the fact that it is an efficient way to damp the structure without adding mass. This is a promising approach, having high applicative potential at long term. Nevertheless, creating well controlled local damping requires understanding in details its behavior. In the case of the ABH, wide-field observation of the interaction with an incident wave front contributes to a better understanding of what is not. Another specificity of the ABH is that it exhibits a large vibration dynamics with high variability in its central area. It also follows that ABH is a good candidate to test experimental measurement methods.

The paper is organized as follows: Section II gives the basics fundamentals of wide-field vibrometry based on digital holography, Section III describes the experimental holographic set-up and Section IV discusses on the complex structure of the study. In Section V experimental results are provided whereas Section VI draws the conclusion of the paper.

2. Wide-field vibrometry

Wide-field vibrometry provides new opportunities for studying vibrations and acoustic phenomena at both their time and space scales and is based on high-speed digital holographic interferometry. Digital holograms are produced from the large-field illumination of the object surface to be studied. Since the complex-valued optical field is recorded in any digital holograms, the optical phase, and then, the optical path difference, can be retrieved and yields the measurement of the displacement field at the illuminated surface. Basically, the digital holograms are obtained by recording, with an image sensor organized as a matrix of pixels, the coherent mixing of the diffracted optical wave from the object surface and a known reference wave. If we note O the wave front from the illuminated object and R the wave front from the reference wave, then the digital hologram can be expressed by Eq. (1) (*means complex conjugate) [48,49]:

$$H = |R|^2 + |O|^2 + R^* O + R O^* . \quad (1)$$

The reference wave is generally written as $R(x,y)=a_R \exp[2i\pi(u_0 x+v_0 y)]$ with $\{u_0,v_0\}$ its spatial frequencies and a_R is a constant. In this paper, the specificity of high-speed holographic vibrometry is that the spatial frequencies of R can be set to $\{u_0,v_0\}=\{0,0\}$, corresponding to the on-axis configuration. This point is discussed in detail in [46] and the reader is invited to have a look at the paper for further details. The illuminated object surface is generally at distance d_0 from the recording sensor which is used without any imaging lens (arrangement known as the Fresnel configuration). The object wave diffracted to the sensor plane can be expressed with the Fresnel approximations by Eq. (2) [49,50] ($i=\sqrt{-1}$):

$$O(x, y, d_0) = -\frac{i}{\lambda d_0}\exp\left(\frac{2i\pi d_0}{\lambda}\right)\exp\left(\frac{i\pi}{\lambda d_0}\left(x^2 + y^2\right)\right) \times \int\int A(X, Y)\exp\left(\frac{i\pi}{\lambda d_0}\left(X^2 + Y^2\right)\right)\exp\left(-\frac{2i\pi}{\lambda d_0}(xX + yY)\right)dXdY\,. \quad (2)$$

The object wave front at the object plane is $A(X,Y)=A_0(X,Y)\exp[i\psi_0(X,Y)]$, λ is the wavelength of light, A_0 is related to the object reflectance and ψ_0 is the optical phase related to the object surface profile and roughness.

From the digitally recorded holograms, the reconstruction of the object field at any distance d_r from the recording plane is given by the discrete Fresnel transform [48]. From the hologram, the numerically reconstructed complex-valued image can be obtained from Eq. (3) [48,49]:

$$A_r = h_F \times FFT\left[H \times h_F\right], \quad (3)$$

where FFT means two-dimensional Fast Fourier Transform and h_F is the Fresnel kernel defined by Eq. (4),

$$h_F(x, y) = \frac{1}{\sqrt{\lambda d_r}}\exp\left(i\pi\frac{d_r}{\lambda} - i\frac{\pi}{4}\right)\exp\left[\frac{i\pi}{\lambda d_r}\left(x^2 + y^2\right)\right]. \quad (4)$$

From the numerical computation of Eq. (3), the amplitude and phase of the diffracted field A_r can be evaluated. When the reconstruction distance is $d_r=-d_0$ the initial object plane is recovered and the phase variation from the time sequence is related to the displacement field at the surface. When considering two consecutive time-instants in the hologram sequence, the phase variation is given by Eq. (5) and is similar to the Doppler effect, but from the point of view of the optical phase. The phase change is thus related to the displacement field **U** rather than the velocity.

$$\Delta\varphi = \frac{2\pi}{\lambda}\mathbf{U}.\left(\mathbf{K}_e - \mathbf{K}_o\right). \quad (5)$$

In Eq. (5), $\mathbf{K_e}$ is the normalized illumination vector from the light source to the object and $\mathbf{K_o}$ is the observation vector (also normalized) from the object to the sensor, both defined in a set of reference axis ($\mathbf{i}$,$\mathbf{j}$,$\mathbf{k}$) attached to the object surface, with $\mathbf{k}$ being perpendicular to the surface. In the approach described in this paper, the observation vector is parallel to $\mathbf{k}$ and the illumination vector is quasi-oriented along $-\mathbf{k}$. Thus, the sensitivity of the phase measurement is oriented along $\mathbf{k}$ so that the out-of-plane movement at the surface of the object, u_z, can be measured. Generally, the phase variation in Eq. (5) is obtained modulo 2π and requires phase unwrapping to yield u_z [51].

Thanks to the coherent mixing by heterodyning with the reference wave (Eq. (1)), the object wave O is amplified by the reference wave R, because of the term R^*O included in the recorded hologram (third term of Eq. (1)). So, a weak object wave, due to a non-cooperative target, may be balanced by a strong reference wave, if $|R|^2>>|O|^2$. In addition, the reference wave is directly impacting the sensor and this makes it easier to get large amount of photons for optimizing light detection. In the approach described in this paper, measurements are possible with about 40% of the full sensor dynamics and ratio $|R|^2/|O|^2$ at about 100, thus yielding suitable phase maps for visualization or metrology purposes.

Image reconstruction according to Eq. (3) imposes the spatial resolution in the image plane. It depends on the sensor-to-object distance, on the pixel pitch of the sensor (p_x) and on the number of pixels of the recorded hologram. If we note $\{M,N\}$ the number of pixels along respectively the vertical and horizontal direction of the sensor plane, then the spatial resolutions achieved using Eq. (4) are given by [49]:

$$\begin{cases} \rho_x = \dfrac{\lambda d_0}{N p_x} \\ \rho_y = \dfrac{\lambda d_0}{M p_x} \end{cases}. \tag{6}$$

It follows that if the recording matrix is not square, the spatial resolution in the image plane is anisotropic. Typically, at frame rate 100kHz, the sensor of the set-up provides N=384 and M=264 pixels.

3. Experimental set-up

The experimental set-up is described in Fig. 1(a). The light is emitted from a continuous DPSS laser at λ=532nm with maximum power at 6W. The laser is separated into a reference wave and an object wave by using a polarizing beam splitter (PBS). The half-wave plate at the output of the laser is used to adjust the power in both object and reference paths to get adequate $|R|^2/|O|^2$ ratio. This ratio is an important parameter of the experimental set-up. In [46] was demonstrated that in order to minimize the influence of measurement noise and to get contrasted phase fringe patterns, the ratio has to be adjusted at around 100. The way to adjust the ratio is as follows: the power meter in Fig. 1(a) placed near the 50% beam splitter cube is used to measure the optical power in the reference beam and in the object beam (by blocking one after the other). Using the half wave plate at the output of the laser, the ratio can be set to around 100 when splitting light in the two arms. The polarization of the object wave is then rotated 90° to be parallel with that of the reference wave, so that interferences may occur. The

reference wave is expanded, spatially filtered using a spatial filter (microscope objective and pinhole), and collimated to produce a smooth plane reference wave impacting the sensor at normal incidence. So, the carrier spatial frequencies along the reference beam are $\{u_0,v_0\}\approx\{0,0\}$, giving the on-line configuration [45].

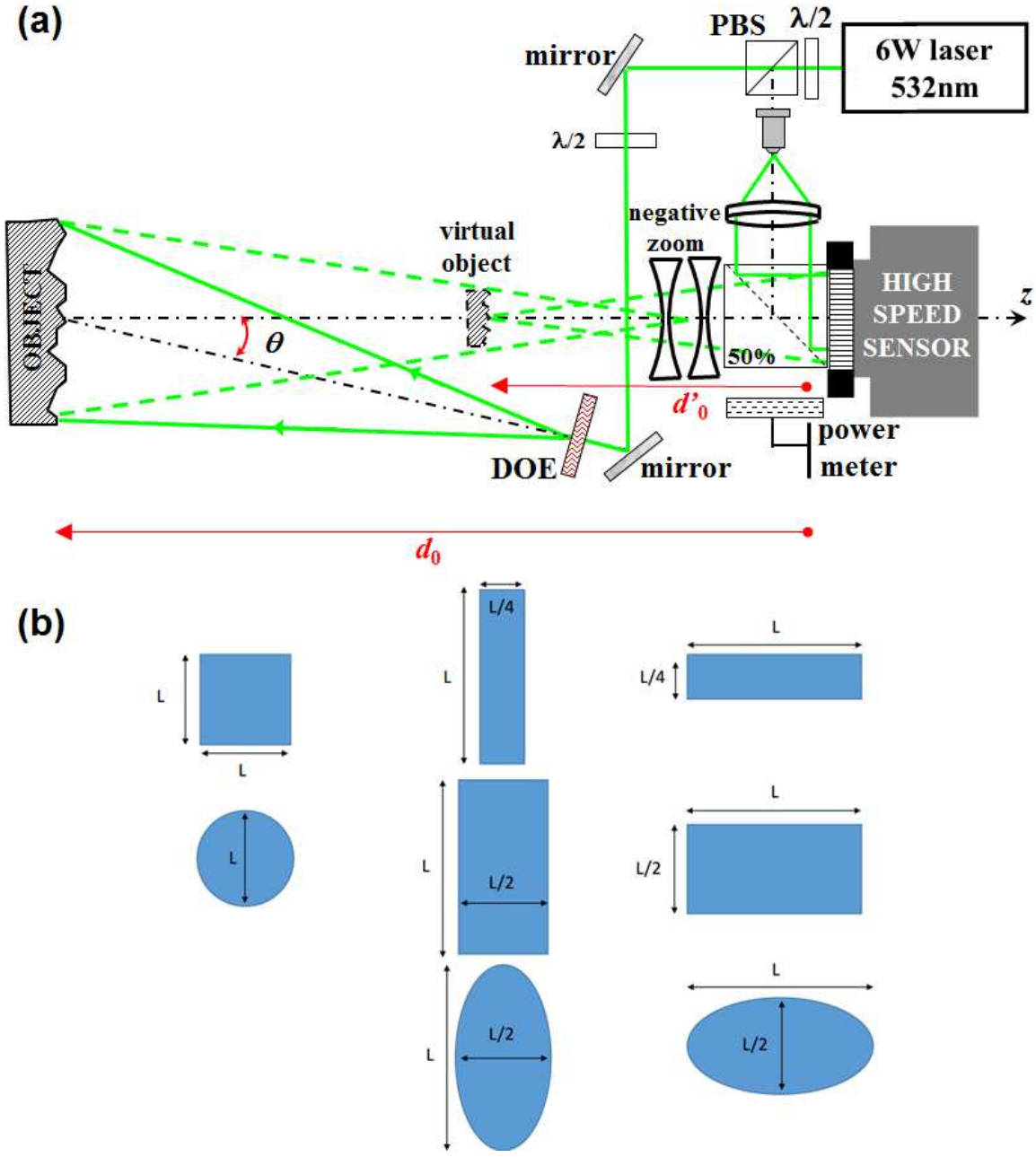

Fig. 1. (a) Experimental set-up for wide-field holographic vibrometry (PBS: polarizing beam splitter, DOE: diffractive optical element, $\lambda/2$ half-wave plate), (b) set of beam shape structures that can be produced by the DOE for illuminating the object surface

The object wave is spatially expanded to illuminate the structure by using a dedicated DOE (Diffractive Optical Element). The DOE inserted in the illumination path is an optical component

that transforms the incident wave front into a desired wave front. It was designed to produce several spot shapes, with 8 subareas, each of them producing a particular laser beam shape. Figure 1(b) illustrates the diversity of shapes that can be produce with the DOE: square area, elliptical areas, narrow and large rectangular beams (vertical and horizontal). Such beam shaping increases the photometric efficiency of the set-up by avoiding wasting light with classical lenses and mirror assembly. In practice, a DOE consists of a substrate (a glass plate for example) on which a photoresist is deposited by spin-coating. The photoresist S1800 series from Micro Resist Technology was used, which is a positive photoresist. This series has different viscosities and therefore permits to put down photoresist layers with different thicknesses ranging from a few hundred nm to above 10microns. The error in the uniformity of the photoresist layer in the spin-coating process is about 20nm. Within this photoresist, micro or nano diffractive structures are engraved [50]. For application in vibroacoustics, centrosymmetric diffractive patterns are required (see Fig. 1(b)). They can be obtained through binary phase DOEs (phase shift of π between the 2 levels), the simplest to produce. The spin-coating speed should be chosen so that the thickness of the photoresist layer is $e=\lambda/2(n-1)$, where n is the refractive index of the photoresist material at the DOE working wavelength λ [52]. In this paper, the illuminating wavelength is 532nm and the photoresist thickness is close to 405nm. To solve the inverse diffractive problem, diffractive structures are modelled using an Iterative Fourier-Transform Algorithm (IFTA) optimization algorithm [53,54]. Once simulated, the DOEs are fabricated in a clean room using a micro-photolithography system developed at IMT Atlantique [55]. In the fabrication process, the parallel direct-write photo-plotter uses a programmable liquid crystal spatial light modulator (SLM) as a reconfigurable mask. The photoresist is then exposed to a pattern (corresponding to the modelled diffractive structures) of intense light with a wavelength of 436nm to which the photoresist is active. A reduction lens is used to image the pattern at LCD into the photoresist layer. The resolution limit of the direct-write photo-plotter is about 750nm. The pattern can be replicated along x and y axes by moving a nano-precision 2D translational stage. This fabrication process has been shown to be cost-effective and particularly adapted to DOE prototyping. After exposure, the substrate is put into a developer solution (Microposit™ 351 developer, Rohm and Haas) to etch the exposed pattern into the photoresist layer. The fabricated structures are then measured with an interferometric microscope, where the lateral dimensions and the etching depth can be verified. The quality of a DOE is assessed depending on the application, usually by diffraction efficiency, uniformity and/or mean-square-error [56,57].

In the set-up, the illumination angle is about θ=15°. From Eq. (5), the out-of-plane displacement field at the surface of the object is given by Eq. (7) [35]:

$$u_z = \frac{\lambda}{2\pi}\frac{\Delta\varphi}{1+\cos(\theta)}. \tag{7}$$

The object and reference waves are combined by the 50% beam splitter cube placed just in front of the high-speed sensor. In the optical path from the object surface to the sensor plane, a negative zoom is inserted, in front of the cube. The negative zoom is a divergent optical system having a negative focal length. The image produced by such optical system is not located in the sensor plane, but at shorter distance from the sensor. This negative zoom produces a smaller image of the object when reducing the object-to-sensor distance [58,59]. This provides a smaller virtual object facing the sensor at smaller distance d'_0. By this way, the dimensions of the virtual object are compatible with the requirement from the Shannon conditions for recording digital holograms [49]. Basically, from the hologram, the virtual image can be computed when setting $d_r=-d'_0$. And the physical plane is obtained by scaling the set of reference coordinates attached to the image plane. If we note g_{opt} the optical magnification ($0<g_{opt}<1$) produced by the negative zoom, then the spatial resolutions in the final image are given by

$$\begin{cases} \rho_x = \dfrac{\lambda d'_0}{N p_x g_{opt}} \\ \rho_y = \dfrac{\lambda d'_0}{M p_x g_{opt}} \end{cases} . \tag{8}$$

The sensor is a high-speed camera from Photron, with pixel pitch at p_x=20µm and maximum spatial resolution including 1024×1024 pixels. At the full spatial resolution, the maximum frame rate is 12500Hz. When increasing the frame rate, the spatial resolution is degraded, that is 328×768 at 50kHz and 264×384 at 100kHz. The exposure time can be set from 380ns to few ms. In this paper, the exposure time was set at 1µs and the laser power was adjusted at 3W. When adjusting the negative zoom to capture holograms from a rectangular area sized 27cm×14cm, about 380cm^2, the focal length was set to –42.8mm, leading to the reconstruction distance at d'_0=–160mm. In this set-up, the distance between the initial object plane and the sensor plane is about 2.45m and the optical magnification is g_{opt}=0.0152. So, at 100kHz, with the experimental parameters the spatial resolutions are respectively given along the x and y direction by

$$\begin{cases} \rho_x = 792\ \mu m \\ \rho_y = 1.06\ mm \end{cases} . \tag{9}$$

4. Plate equipped with a 2D ABH

Wide-field holographic vibrometry is applied to the visualization of travelling waves propagating in a plate equipped with a 2D ABH, when exciting using an impact hammer. From Mironov [1] and Krylov [2], the ABH is known to provide an efficient vibration damper for flexural waves on panels when the wave trap is made with a local variation of the thickness. Generally, the truncation effect near the ABH extremity can be overcome by adding a thin damping layer in its vicinity [2]. For building panels with damping properties, the circular geometry of ABH was proposed and developed in [3,4]. We manufactured a 2D ABH in alloy plate sized 900mm×540mm with 1.5mm thickness. The ABH zone is ϕ=59mm in diameter and is located at 196mm from the left edge and 375mm from the top of the plate. The center of the ABH is open with 9mm diameter. The plate equipped with the ABH and the thickness profile of typical 2D ABH are depicted in Fig. 2.

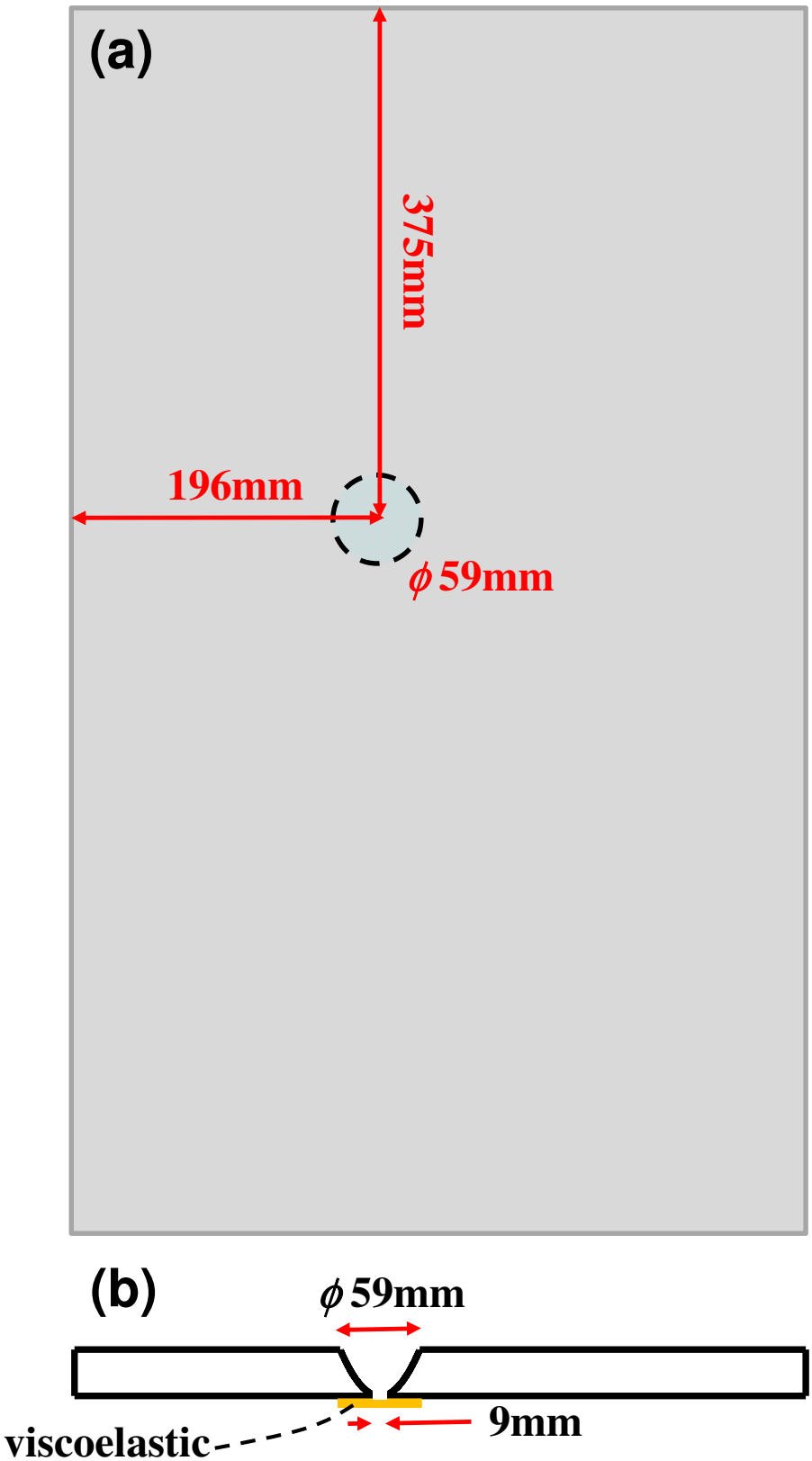

Fig. 2. (a) Scheme of the plate equipped with the 2D ABH, (b) profile of the plate equipped with the 2D ABH with details of the shape of the structure and the thin viscoelastic layer (in orange color) stuck at the ABH center

The principle of the ABH effect is as follows: the extremity of the structure is shaped so that the local phase velocity of flexural wave decreases progressively to 0. The consequence is that the ABH area behaves as a trap for the wave propagating through, leading to energy absorption and thus avoiding reflection phenomenon from the ABH. Figure 2(a) shows an overview of the plate equipped with the 2D ABH and its location in the plane of the plate. In the ABH area, the local thickness decreases with a power law profile as proposed by Mironov (quadratic profile) [1]. This means that the center of the ABH area is shaped so that its thickness $h(x)$ progressively decreases to 0 according to Eq. (9):

$$h(x) = \begin{cases} e_0 (x - x_0)^2 & \textbf{if } |x - x_0| \le \phi / 2 \\ e_0 & \textbf{if not} \end{cases} . \quad (9)$$

In Eq. (9), x_0 is the center of the ABH area and ϕ its diameter, whereas e_0 is the initial thickness of the plate. A thin viscoelastic damping layer (a viscoelastic tape having a thickness at few 20-50µm) has been added in the center of the ABH area. The system constituted by the ABH and the viscoelastic layer is what is usually called a "practical ABH": in the studied case, preliminary tests show that it is able to damp vibration from a cut-on frequency of about 500-600Hz.

5. Experimental results

In the case presented in this paper, one aims at visualizing the transient acoustic waves propagating in the structure equipped with the 2D ABH, and excited by transient signal. Therefore, the plate was excited with an impact hammer from PCB Piezotronics (ref. 086E80), equipped with a force sensor, the tip being equipped with a stiff PVC tip. The hammer is used to provide shocks to the structure. The stiff tip permits to get a broad range of frequency, typically up to 10kHz. The impact of the hammer is localized at 170mm from the right edge of the plate and 292mm from its top, thus 38mm above the illuminated area. Figure 3(a) shows the force signal recorded with the set-up. The maximal force is about 8N. The duration of the shock is about 50µs (estimated at half width). The power spectrum density of the force signal injected in the plate is provided in Fig. 3(b). As can be seen, the spectrum is broad and flat up to almost 10kHz. The force sensor is used to trig the sensor in order to record a hologram sequence. A sequence including 37600 digital holograms was recorded at the sensor frame rate of 100kHz that is duration about 0.376s, with time shift between two consecutive holograms at 10µs. Considering the frequency bandwidth in Fig. 1(b), the Shannon conditions are fulfilled for the hologram temporal recording. Indeed, the frame rate

of the sensor is at 100kHz and the bandwidth of the shock is 20kHz. So, the temporal recording provides at least 5 sampling points for the maximum frequency in the temporal excitation signal.

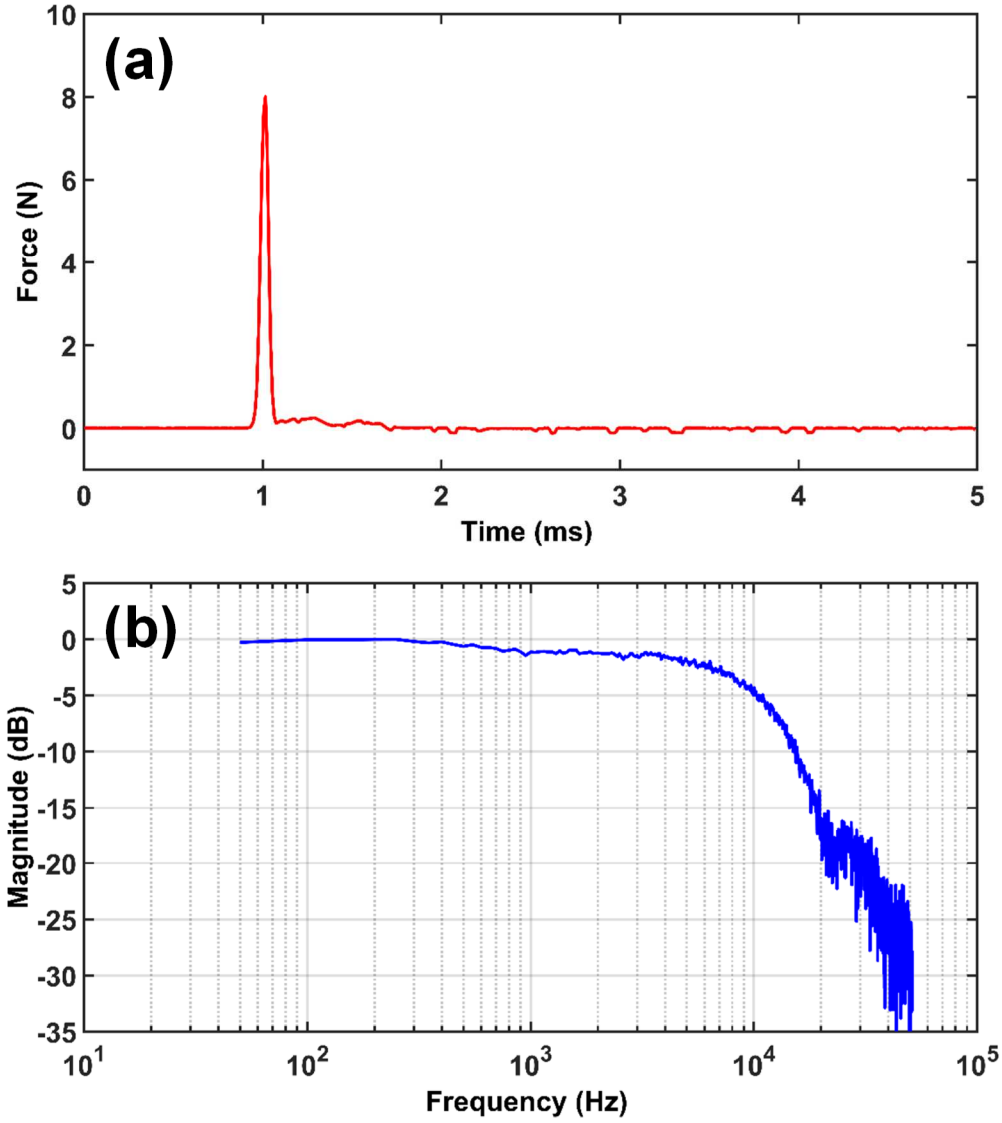

Fig. 3. (a) Force signal injected in the plate, (b) power spectrum density of the force signal

The digital holograms are reconstructed using the algorithm described in Eq. (3) with computation over 1024×1024 data points [49]. Figure 4(a) shows a picture of the plate illuminated with the horizontal rectangular laser shape. The ABH area is indicated by a dashed red line and the position of the impact hammer is marked by the red spot. Note that, in the plate, there is a screw in the illuminated area, which was used to clamp a mechanical shaker in previous experiments and which does not have specific role in the proposed set-up. Interestingly, the influence of this small screw can be seen by the measurement method. Figure 4(b) shows the amplitude image reconstructed from digital holograms. The illuminated

area marked with the dashed red line can be clearly observed. The ABH area, the hammer position and the screw are also indicated.

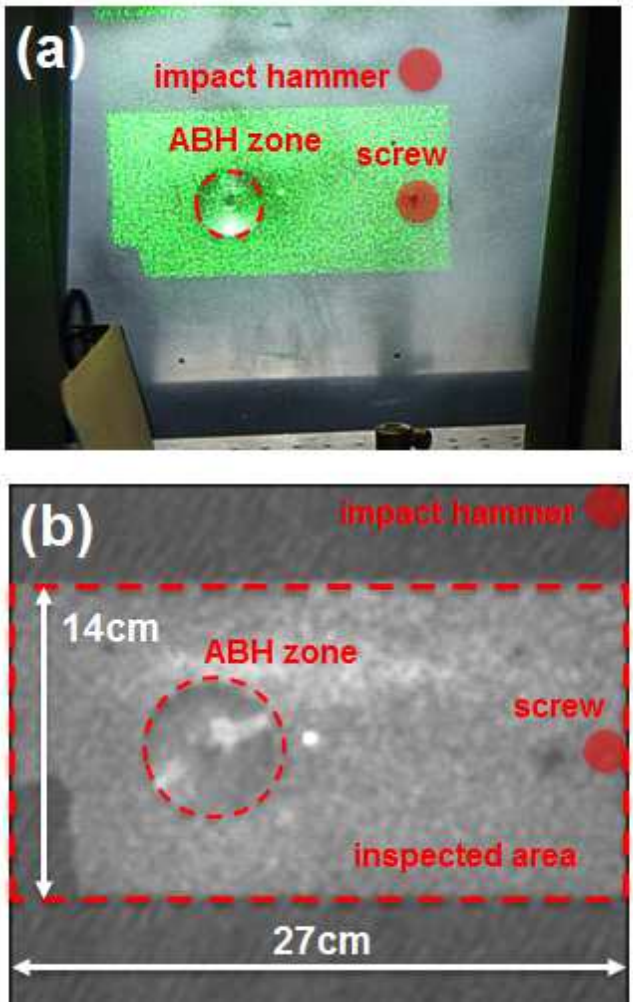

Fig. 4. (a) Picture of the plate illuminated with the rectangular laser shape, the ABH area is indicated by a dashed red line and the position of the impact hammer is marked by the red spot, (b) amplitude image reconstructed from digital holograms, the illuminated area is marked with the dashed red line

With the spatial resolution evaluation from Eq. (8), the dashed red lined area in Fig. 4(b) is covered by 353×132 independent data points, thus providing a collection of 46600 measurement points at the surface of the plate. From the complex valued data computed from the reconstruction algorithm, the optical phase at each time instant can be extracted and the phase difference can be obtained. Optical phase differences are obtained modulo 2π and they need to be unwrapped [51] to get the scaled physical displacement field according to Eq. (7). However, modulo 2π phase variations are helpful for visualizing the interaction between the 2D ABH and the wave front emitted from the shock with the impact hammer. Indeed, the phase is wrapped in the interval $[-\pi,+\pi]$ and that permits to keep the dynamic range of display constant over the set of figures, even if the wave amplitude is weak. But, in order to also

provide amplitude maps, the wave amplitude was calculated and displayed after unwrapping the modulo 2π phase data according to Eq. (7) with λ=532nm and θ=15°. In the followings, Figure 5 to Fig. 9 show several sets of modulo 2π phase maps extracted from the phase variation sequence after computation from the recorded digital holograms. In Fig. 5 to Fig. 9, the dashed black circle indicates the ABH area. Fig. 10 to Fig. 12 show amplitude maps from Fig. 6 to Fig. 8, with the dynamic range adjusted to ±220nm.

Figure 5(a) to Fig. 5(f) show six phase maps corresponding to the time interval [0ms; 0.05ms] and showing the first instants of the wave front arrival in the region of interest illuminated by the laser. The spherical wave front emitted from the impact point and propagating through the plate at the early first instants can be observed. After 0.12ms the wave front reaches the screw screwed to the plate. Figure 6(a) to Fig. 6(f) exhibit the interaction between the wave front and the screw. One can clearly observe both phenomena: reflection and diffraction of the wave by the screw. Figure 6(b) to Fig. 6(e) show the diffraction by the screw.

Figure 7(a) to Fig. 7(f) provides pictures of the wave front when entering in the ABH area. The vanguard of the wave front impacts the area 0.19ms after the shock. Considering the gradient of velocity in the ABH area, this part of the wave front has its velocity decreased. The wave front is then distorted and this can be observed in the sequence of pictures in Fig. 7. In Fig. 7(c), 0.21ms after the shock, the incident wave front is deformed by the velocity gradient in the ABH area: the local curvature of the wave front in the ABH area changes its sign. In Fig. 7(e) and Fig. 7(f), respectively 0.23ms and 0.24ms after the shock, one can observe the dislocation of the wave front in the ABH zone. Note that one observes concentrated phase jumps in the ABH center which indicate that the local vibration amplitude increases. These phase jumps are not spatially resolved. It follows that in Fig. 10 to Fig. 12 displaying the amplitude of the vibration, the quantitative data are not relevant in the ABH circled area. This is well correlated with works at LAUM demonstrating the high concentration of vibration energy at the edges of the 2D ABH [12]. Note that in order to observe the wave front dislocation with better spatial resolution, one would have to change the experimental optical parameter in order to get a more focused imaged area, to yield resolved phase jumps in the ABH center. Figure 8 shows a set of modulo 2π phase maps showing the vibration field few instants after the wave front passed through the ABH area, in between 0.31ms and 0.36ms after the shock. The deformation of the wave front in the lower-left part of the field of view can be observed, whereas the ABH center part exhibits non resolved phase jumps which indicate local high vibration amplitude. After a while, about

16ms after the shock, at the periphery of the ABH, a vibration field with lower amplitude is observable, whereas the center still exhibits phase jumps indicating local high vibration amplitude. This is highlighted in Fig. 9(a) to Fig. 9(f) which show the sequence of pictures 15.95ms to 16ms after the shock.

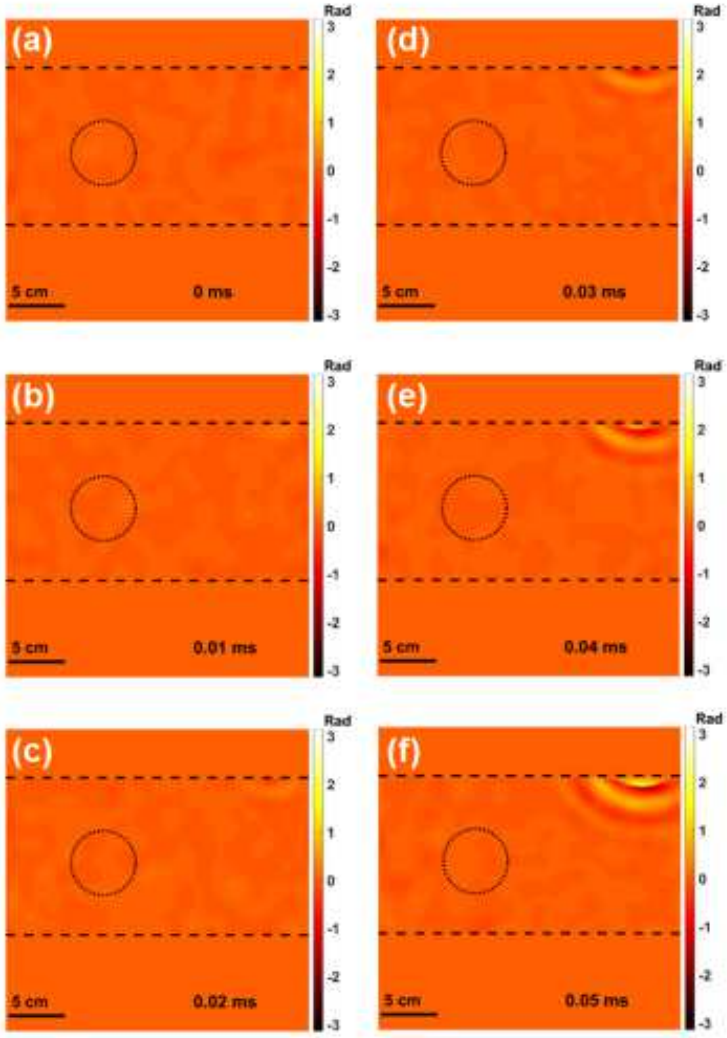

Fig. 5. Extracted modulo 2π phase maps over time interval [0ms; 0.05ms] showing the first instants of the wave front arrival in the region of interest illuminated by the laser

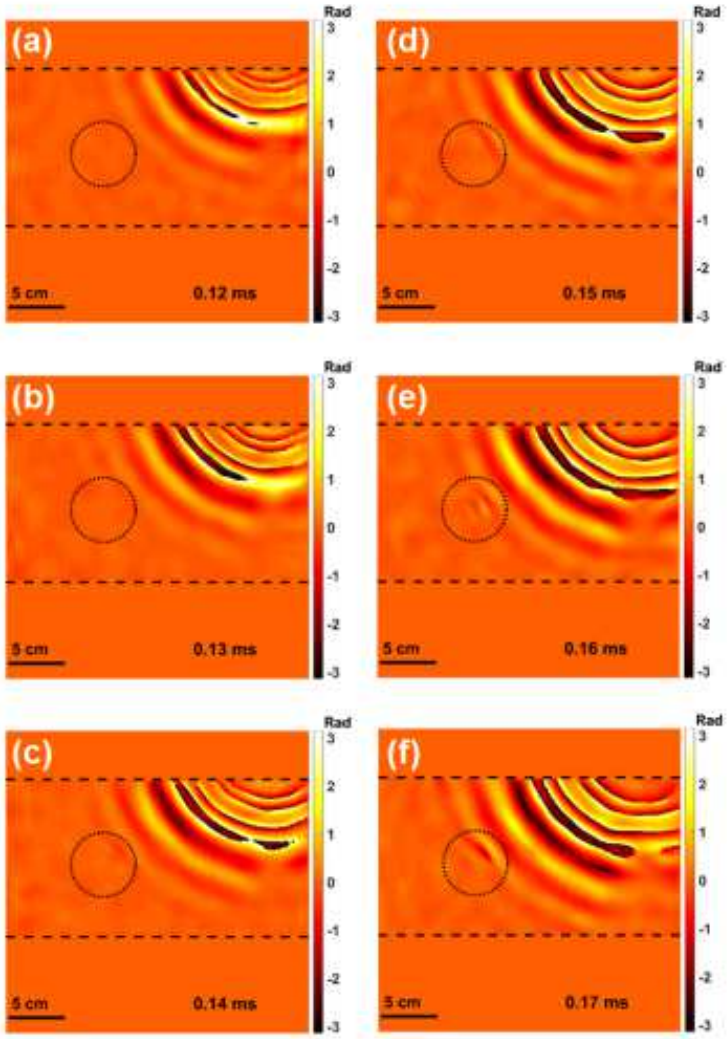

398

399 Fig. 6. Extracted modulo 2π phase maps over time interval [0.12ms; 0.17ms] showing the wave front interacting
400 with the screw inserted in the plate; the reflection of the wave front onto the screw can be visualized

401

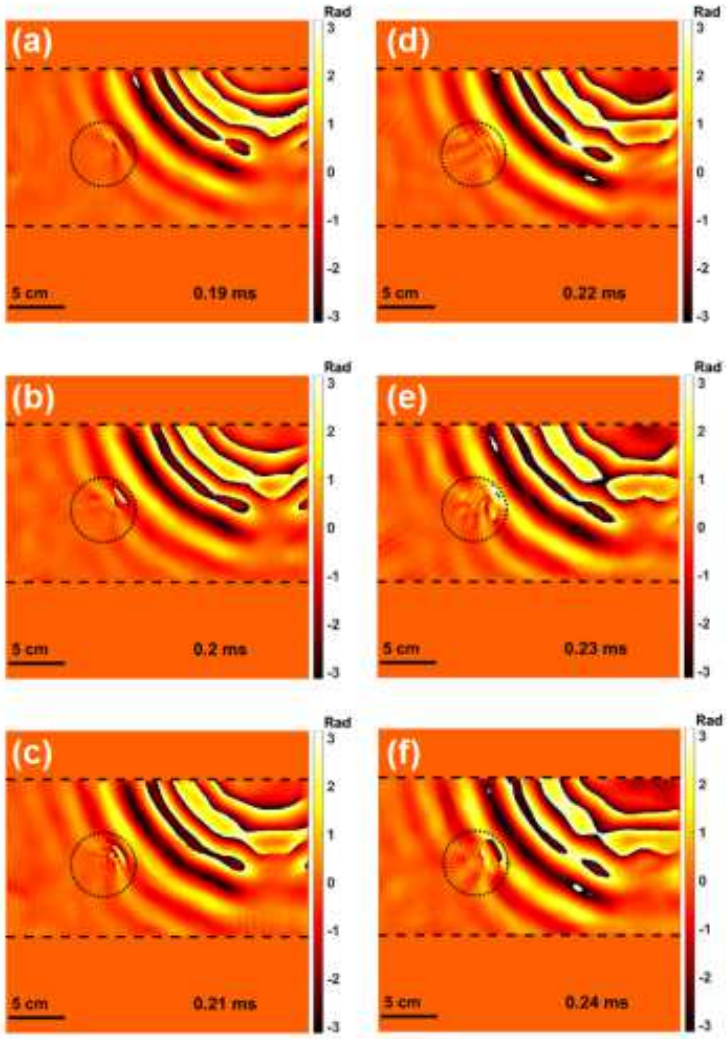

Fig. 7. Extracted modulo 2π phase maps over time interval [0.19ms; 0.24ms] showing the wave front interacting with the ABH area; the distortion of the wave front due to the velocity gradient is visualized

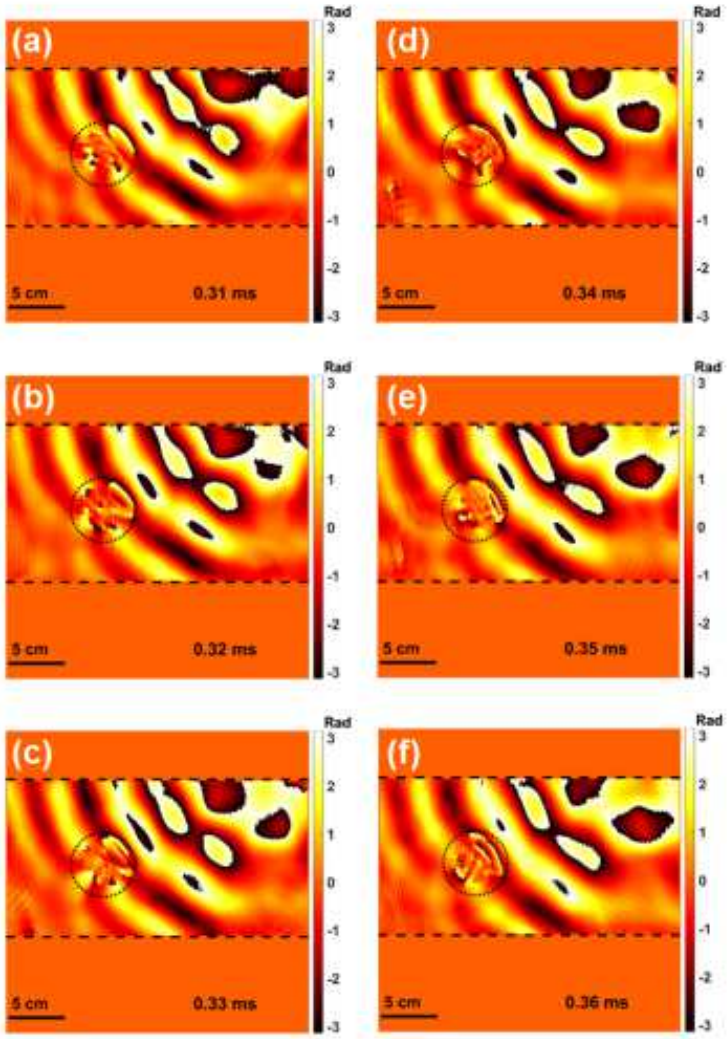

406

407 Fig. 8. Extracted modulo 2π phase maps over time interval [0.31ms; 0.36ms] showing the vibration field few

408 instants after the wave front passed through the ABH area

409

410

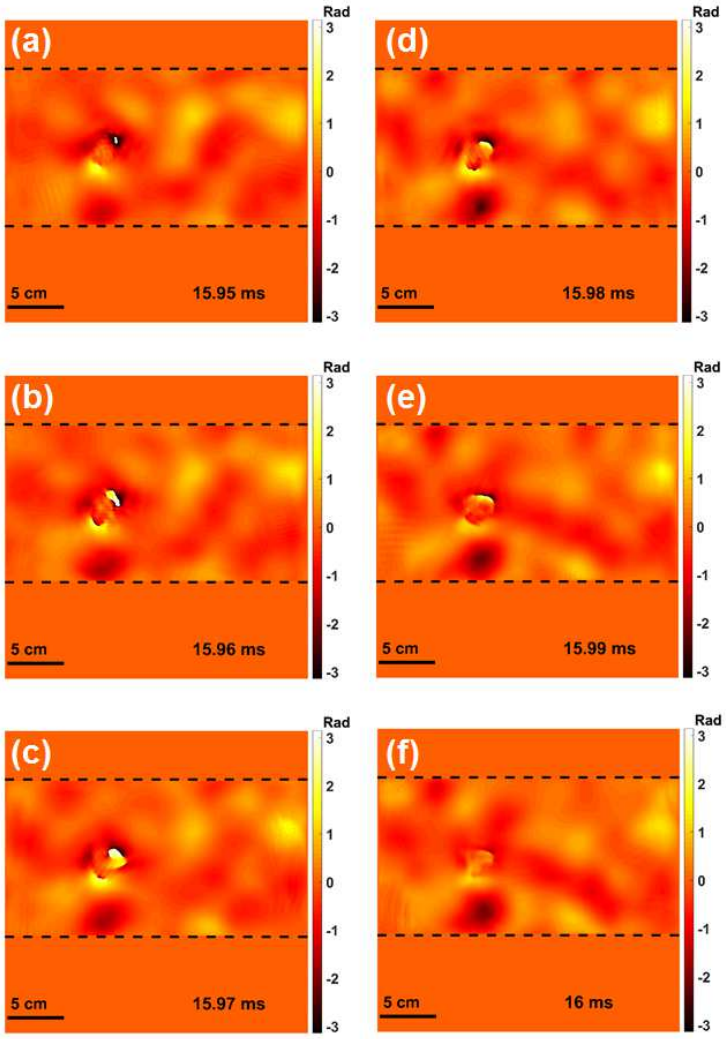

411

412 Fig. 9. Extracted modulo 2π phase maps over time interval [15.95ms;16.00ms] showing the vibration field with
413 lower amplitude around the ABH, whereas the ABH center still exhibits phase jumps indicating local high
414 vibration amplitude

415

416 Supplementary material is provided through the movie of the wave propagating in the plate
417 from which are extracted Fig. 5 to Fig. 9.

418

419

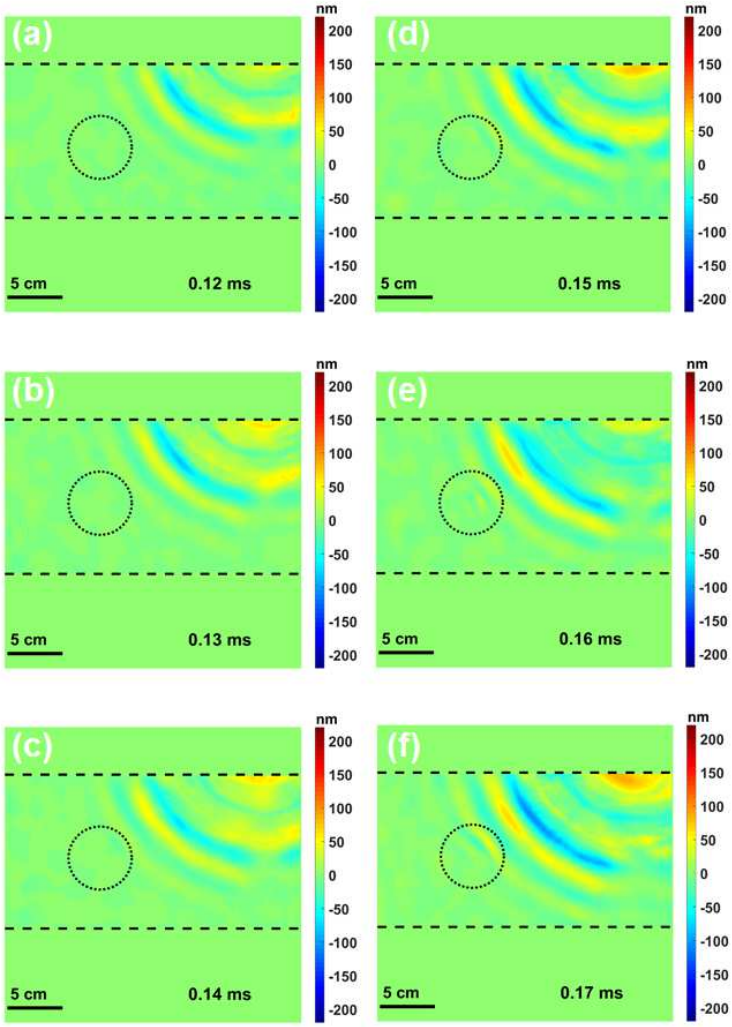

420

421 Fig. 10. Amplitude maps corresponding to Fig. 6, over time interval [0.12ms; 0.17ms], showing the wave front
422 interacting with the screw inserted in the plate

423

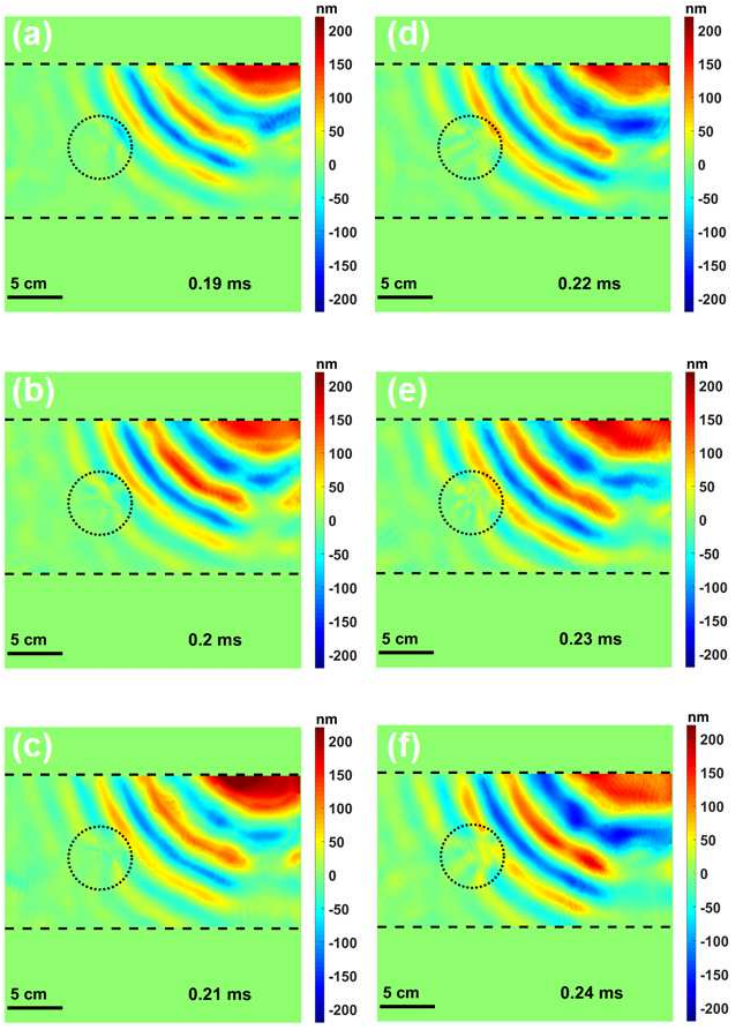

424

425 Fig. 11 Amplitude maps corresponding to Fig. 7, over time interval [0.19ms; 0.24ms] showing the wave front
426 interacting with the ABH area; the distortion of the wave front due to the velocity gradient is visualized

427

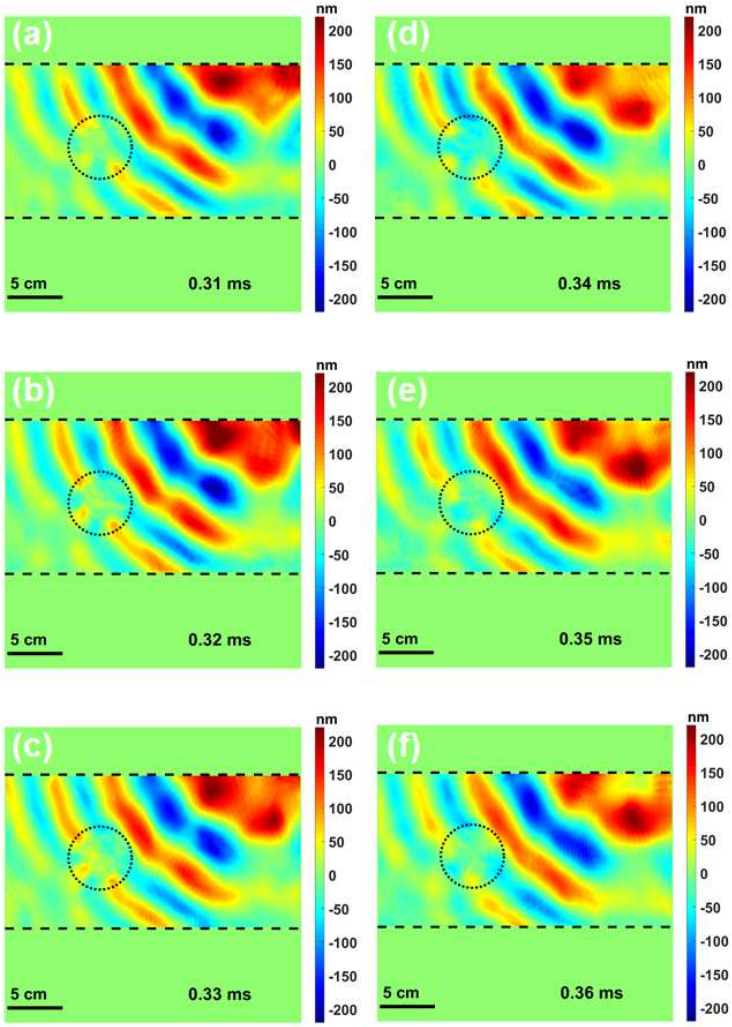

Fig. 12. Amplitude maps corresponding to Fig. 8, over time interval [0.31ms; 0.36ms] showing the vibration field few instants after the wave front passed through the ABH area

The set of sequences, provided through Fig. 5 to Fig. 9, Fig. 10 to Fig. 12, and supplementary material, yields an operational analysis through highlighting the wave front propagating in this complex environment. High-speed digital holographic vibrometry experimentally demonstrates such complex phenomena, at both its time (0~16ms, and later if needed) and space scale (~380cm^2). As a result, the wide-field and real-time investigation of the propagation of waves in ABH inhomogeneous wave guide can be envisaged in the near future.

6. Conclusion

This paper presents and discusses the application of a robust and efficient digital holographic set-up including a compact interferometer with the Fresnel configuration equipped with a

443 negative zoom and a diffractive optical element (DOE) to improve the photometric efficiency
444 of the set-up for illuminating large surfaces. We demonstrate the possibility of measuring
445 transient vibrations of structures at 100kHz frame rate when providing quantitative data on
446 380cm^2 rectangular spot at the object surface. This is the best performance ever achieved for
447 such area and frame rate, to the best of our knowledge. This paper provides the investigation
448 of traveling acoustic waves propagating in alloy plate equipped with a two-dimensional
449 Acoustic Black Hole (ABH). The wave front is generated by an impact hammer to yield 8N
450 force with duration about 50μs. The time sequence of the vibration field obtained after the
451 shock is depicted and exhibits the propagation of the wave front in the complex structure
452 made of the plate equipped with the ABH, and containing a screw. It follows that the
453 observation of the modification of the wave propagation can be observed at very short time
454 scale. Diffraction and reflection phenomena can be clearly seen when the wave front reaches
455 the screw. The modification of the wave front due to the gradient in elastic properties related
456 to the ABH area is also highlighted. Observations are well correlated to theoretical
457 approaches of literature.
458 The approach presented in the paper opens the way to a thorough analysis of physical
459 phenomena existing in and around the ABH, such as for example non-linear behavior in the
460 center of the ABH, or qualifying the efficiency of the wave trap by evaluating its reflection
461 coefficient. In addition, one might be able to address other problems which cannot be
462 addressed by classical experimental means such as vibrations of panels induced by hydro or
463 aero-acoustic sources, structural vibration induced by squeak and rattle noise.
464

465 **Acknowledgments**

466 The authors would like to express their appreciation to Prof. François Gautier and Dr. Adrien
467 Pelat from LAUM CNRS at Le Mans University for very fruitful discussion and comments.
468 This study is part of the Chair program VIBROLEG (Vibroacoustics of Lightweight
469 structures) supported by IRT Jules Verne (French Institute in Research and Technology in
470 Advanced Manufacturing Technologies for Composite, Metallic and Hybrid Structures). The
471 authors wish to associate the industrial and academic partners of this project; respectively

Airbus, Alstom Power, Bureau Veritas, CETIM, Daher, DCNS Research, STX and Le Mans University in France.

References

1. M.A. Mironov. “Propagation of a flexural wave in a plate whose thickness decreases smoothly to zero in a finite interval,” *Sov. Phys.: Acoustics*, **34**(3), 318-319 (1988).
2. V.V. Krylov, and F.J.B.S. Tilman, “Acoustic 'black holes' for flexural waves as effective vibration dampers,” *Journal of Sound and Vibration* **25**, 605-619 (2004).
3. E.P. Bowyer, D.J. O’Boy, V.V. Krylov, and F. Gautier, “Experimental investigation of damping flexural vibrations in plates containing tapered indentations of power-law profile,” *Applied Acoustics* **74**, 553-560 (2013).
4. V.B. Georgiev, J. Cuenca, F. Gautier, L. Simon, and V.V. Krylov, “Damping of structural vibrations in beams and elliptical plates using the acoustic black hole effect” *Journal of Sound and Vibration* **330**, 2497-2508 (2011).
5. V. Denis, F. Gautier, A. Pelat, and J. Poittevin, “Measurement and modelling of the reflection coefficient of an Acoustic Black Hole termination,” *Journal of Sound and Vibration* **349**, 67-79 (2015).
6. V. Denis, A. Pelat, and F. Gautier, “Scattering effects induced by imperfections on an acoustic black hole placed at a structural waveguide termination,” *Journal of Sound and Vibration* **362**, 56-71 (2016).
7. L. Tang, L. Cheng, H. Ji, and J. Qiu, “Characterization of acoustic black hole effect using a one-dimensional fully-coupled and wavelet-decomposed semi-analytical model,” *Journal of Sound and Vibration* **374**, 172-184 (2016).
8. Y. Lee and W. Jeon, “Vibration damping using a spiral acoustic black hole,” *Journal of the Acoustical Society of America* **141**(3), 1437-1445 (2017).

9. W. Huang, H. Ji, J. Qiu, and L. Cheng, “Analysis of ray trajectories of flexural waves propagating over generalized acoustic black hole indentations,” *Journal of Sound and Vibration* **417**, 216-226 (2018).
10. W. Huang, H. Ji, J. Qiu, and L. Cheng, “Wave energy focalization in a plate with imperfect two-dimensional acoustic black hole indentation,” *Journal of Sound and Vibration*, Transactions of the ASME **138**(6), (2016).
11. E.P. Bowyer and V.V. Krylov, “Damping of flexural vibrations in turbofan blades using the acoustic black hole effect,” *Applied Acoustics* **76**, 359-365 (2014).
12. O. Aklouche, A. Pelat, S. Maugeais, and F. Gautier, “Scattering of flexural waves by a pit of quadratic profile inserted in an infinite thin plate,” *Journal of Sound and Vibration* **375**, 38-52 (2016).
13. J. Bayod, “Application of elastic wedge for vibration damping of turbine blade,” *Journal of System Design and Dynamics* **5**, 1167-1175 (2011).
14. V. Denis, A. Pelat, C. Touze, and F. Gautier. “Improvement of the acoustic black hole effect by using energy transfer due to geometric nonlinearity,” *International Journal of Non-Linear Mechanics* **94**, 134-145 (2017).
15. H. Li, C. Touzé, A. Pelat, F. Gautier, X. Kong, “A vibro-impact acoustic black hole for passive damping of flexural beam vibrations,”*Journal of Sound and Vibration* **450**, 28-46 (2019).
16. S.C. Conlon, J.B. Fahnline, and F. Semperlotti, “Numerical analysis of the vibroacoustic properties of plates with embedded grids of acoustic black holes,” *Journal of the Acoustical Society of America* **137**, 447-457 (2015).
17. O. Aklouche, A. Wang, A. Pelat, and F. Gautier, “Dispersion curves for bending waves in a meta-plate made with a periodic lattice of abh like scatterers,” *INTER-*

522 *NOISE and NOISE-CON Congress and Conference Proceedings* **255**, 5226-5232
523 (2017).
524 18. L.E. Drain, *The laser Doppler technique* (Chichester, New York, Wiley, 1980).
525 19. C.B. Scruby, and L.E. Drain, *Laser-ultrasonics: techniques and applications* (Bristol,
526 UK, Adam Hilger, 1990).
527 20. J.-P. Monchalin, "Progress towards the application of laser-ultrasonics in industry,"
528 In: D.O. Thompson & D.E. Chimenti, editors, *Review of progress in quantitative*
529 *nondestructive evaluation*, **12**. 495, New York: Plenum (1993).
530 21. P. Castellini, G.M. Revel, and E.P. Tomasini, "Laser doppler vibrometry: a review of
531 advances and applications," *Shock. Vib. Dig.* **30**, 443-456 (1998).
532 22. W. MacPherson, M. Reeves, D. Towers, A. Moore, J. Jones, M. Dale, and C.
533 Edwards, "Multipoint laser vibrometer for modal analysis," *Applied Optics* **46**, 3126-
534 3132 (2007).
535 23. K. Sun, L. Yuan, Z. Shen, Z. Xu, Q. Zhu, X. Ni, and J. Lu, "Scanning laser-line source
536 technique for nondestructive evaluation of cracks in human teeth," *Applied Optics***53**,
537 2366-2374 (2014).
538 24. M. Connelly, P. Szecówka, R. Jallapuram, S. Martin, V. Toal, and M. Whelan,
539 "Multipoint laser Doppler vibrometry using holographic optical elements and a CMOS
540 digital camera," *Optics Letters* **33**, 330-332 (2008).
541 25. Y. Fu, M. Guo, and P. Phua, "Multipoint laser Doppler vibrometry with single
542 detector: principles, implementations, and signal analyses," *Applied Optics* **50**, 1280-
543 1288 (2011).
544 26. Y. Fu, M. Guo, and P. Phua, "Spatially encoded multibeam laser Doppler vibrometry
545 using a single photodetector," *Optics Letters* **35**, 1356-1358 (2010).

546 27. P. Picart, J. Leval, D. Mounier, and S. Gougeon, “Time averaged digital holography,”
547 *Optics Letters* **28**, 1900-1902 (2003).
548 28. A. Asundi, and V. Raj Singh, “Amplitude and phase analysis in digital dynamic
549 holography," *Optics Letters* **31**, 2420-2422 (2006).
550 29. M. Leclercq, M. Karray, V. Isnard, F. Gautier, and P. Picart, “Evaluation of surface
551 acoustic waves on the human skin using quasi-time-averaged digital Fresnel
552 holograms,” *Applied Optics* **52**, A136-A146 (2013).
553 30. B.P. Thomas, S. Annamala Pillai, and C.S. Narayanamurthy, “Investigation on
554 vibration excitation of debonded sandwich structures using time-average digital
555 holography,” *Applied Optics* **56**(13), F7-F13 (2017).
556 31. B.P. Thomas, S. Annamala Pillai, and C.S. Narayanamurthy, “Digital holographic
557 study on the dynamic response of plates with geometric and material discontinuities
558 simulating potted-insert metallic honeycomb sandwich structures,” *Applied Optics*
559 **58**(5), A33-A40 (2019).
560 32. M. Stipčević, N. Demoli, H. Skenderović, M. Lončarić, A. Radman, J. Gladić, and D.
561 Lovrić, “Effective procedure for determination of unknown vibration frequency and
562 phase using time-averaged digital holography,” *Optics Express* **25**(9), 10241-10254
563 (2017).
564 33. M. Kirkove, S. Guérit, L. Jacques, C. Loffet, F. Languy, J.F. Vandenrijt, and M.
565 Georges, “Determination of vibration amplitudes from binary phase patterns obtained
566 by phase-shifting time-averaged speckle shearing interferometry,” *Applied Optics*
567 **57**(27), 8065-8077 (2018).
568 34. F. Languy, J.F. Vandenrijt, C. Thizy, J. Rochet, C. Loffet, D. Simon, and M. Georges,
569 “vibration mode shapes visualization in industrial by real-time time-averaged phase-

570 stepped electronic speckle pattern interferometry at 10.6μm and shearographie at
571 532nm," *Optical Engineering* **55**(12), 121704 (2016).
572 35. P. Picart, J. Leval, F. Piquet, J.-P. Boileau, Th. Guimezanes, and J.-P. Dalmont,
573 "Tracking high amplitude auto-oscillations with digital Fresnel holograms," *Optics*
574 *Express* **15**, 8263-8274 (2007).
575 36. G. Pedrini, S. Schedin, and H.J. Tiziani, ''Pulsed digital holography combined with
576 laser vibrometry for 3D measurements of vibrating objects,'' *Optics & Lasers*
577 *Engineering* **38**, 117-129 (2002).
578 37. I. Alexeenko, M. Gusev, and V. Gurevich, "Separate recording of rationally related
579 vibration frequencies using digital stroboscopic holographic interferometry," *Applied*
580 *Optics* **48**, 3475-3480 (2009).
581 38. D. De Greef, J. Soons, and J.J.J. Dirckx, ''Digital stroboscopic holography setup for
582 deformation measurement at both quasi-static and acoustic frequencies,'' *Int. J. of*
583 *Optomechatronics* **8**, 275-291 (2014).
584 39. C. Pérez-López, M. De la Torre-Ibarra, and F. Mendoza Santoyo, "Very high speed
585 cw digital holographic interferometry", *Optics Express* **14**, 9709-9715 (2006).
586 40. M. Khaleghi, J. Guignard, C. Furlong, and J.J. Rosowski, "Simultaneous full-field 3-D
587 vibrometry of the human eardrum using spatial-bandwidth multiplexed holography,"
588 *Journal of Biomedical Optics* **20**, 111202 (2015).
589 41. U. Bortolozzo, D. Dolfi, J.P. Huignard, S. Molin, A. Peigné, and S. Residori, "Self-
590 adaptive vibrometry with CMOS-LCOS digital holography," *Optics Letters* **40**(7),
591 1302-1305 (2015).
592 42. B. Redding, A. Davis, C. Kirkendall, and A. Dandridge, "Measuring vibrational
593 motion in the presence of speckle using off-axis holography," *Applied Optics* **55**(6),
594 1406-1411 (2016).

595 43. M. Ney, A. Safrani, and I. Abdulhalim, "Three wavelengths parallel phase-shift
596 interferometry for real-time focus tracking and vibration measurement," *Optics Letters*
597 **42**(4), 719-722 (2017).
598 44. T. Kakue, Y. Endo, T. Nishitsuji, T. Shimobaba, N. Masuda, and T. Ito, "Digital
599 holographic high-speed 3D imaging for the vibrometry of fast-occurring phenomena,"
600 *Scientific Reports* **7**, 10413 (2017).
601 45. J. Poittevin, P. Picart, C. Faure, F. Gautier, and C. Pézerat, "Multi-point vibrometer
602 based on high-speed digital in-line holography," *Applied Optics* **54**, 3185-3196 (2015).
603 46. J. Poittevin, P. Picart, F. Gautier, and C. Pézerat, "Quality assessment of combined
604 quantization shot-noise-induced decorrelation noise in high-speed digital holographic
605 metrology," *Optics Express* **23**, 30917-30932 (2015).
606 47. J. Poittevin, C. Faure, J. Lemeur, K. Heggarty, C. Pézerat, and P. Picart, "Combined
607 digital-DOE holographic interferometer for force identification in vibroacoustics,"
608 *Proc. SPIE* **10677**, 106773A (2018).
609 48. U. Schnars, and W. Jüptner, ''Direct recording of holograms by a CCD target and
610 numerical reconstruction,'' *Applied Optics* **33**, 179-181 (1994).
611 49. P. Picart, and J. Leval, "General theoretical formulation of image formation in digital
612 Fresnel holography," *Journal of the Optical Society of America* A **25**, 1744-1761
613 (2008).
614 50. J.W. Goodman, *Introduction to Fourier optics* (New York, McGraw-Hill, 1996).
615 51. D.C. Ghiglia, and M.D. Pritt, *Two-dimensional phase unwrapping: theory, algorithms*
616 *and software* (Wiley, New York, 1998).
617 52. D.C. O'Shea, T.J. Suleski, A.D. Kathman, and D.W. Prather, *Diffractive optics:*
618 *Design, Fabrication, and Test* (SPIE Press, 2004).

53. F. Wyrowski, "Diffractive optical elements: iterative calculation of quantized, blazed phase structures," *Journal of the Optical Society of America* A **7**, 961-969 (1990).

54. F. Wyrowski and O. Bryngdahl, "Iterative Fourier-transform algorithm applied to computer holography," *Journal of the Optical Society of America* A **5**, 1058-1065 (1988).

55. M.V. Kessels, M. El Bouz, R. Pagan, and K. Heggarty, "Versatile stepper based maskless microlithography using a liquid crystal display for direct write of binary and multilevel microstructures," J. Micro/Nanolith. MEMS MOEMS **6**, 033002 (2007).

56. B.C. Kress and P. Meyrueis, *Applied digital optics: from micro-optics to nanophotonics* (John Wiley & Sons, Ltd 2009).

57. H.P. Herzig, *Micro-optics: elements, systems and applications* (CRC Press 1997).

58. U. Schnars, T.M. Kreis and W. Jüptner, "Digital recording and numerical reconstruction of holograms: reduction of the spatial frequency spectrum," *Optical Engineering* **35**, 977-982 (1996).

59. J. Mundt and T. Kreis, "Digital holographic recording and reconstruction of large scale objects for metrology and display," *Optical Engineering* **49**, 125801-1-6 (2010).